buildings

MDPI

Article

Fracture *K* Value of Pre-Coated Concrete-Epoxy Mortar Interface Based on a Proposed Bilinear Softening Model

Zhenyuan Hang [1,2], Zhukun Mi [3] and Ying Yu [2,4,*]

[1] College of Road and Bridge, Zhejiang Institute of Communications, Hangzhou 311112, China; hzy1414@126.com
[2] Department of Civil Engineering, Shantou University, Shantou 515063, China
[3] Centre for Innovative Structures, College of Civil Engineering, Nanjing Tech University, Nanjing 211816, China; mizhukun6618@163.com
[4] Guangdong Engineering Center for Structure Safety and Health Monitoring, Shantou University, Shantou 515063, China
* Correspondence: yuying@stu.edu.cn

Abstract

To study the fracture performance of the concrete-epoxy mortar interface (CEMI) pre-coated with epoxy solutions with different concentrations, a total of nine specimens were fabricated to be subjected to four-point bending tests. DIC technology was used to monitor the deformation of the pure bending region of specimens. A triple-fold stiffness model was developed based on the test results of applied load–displacement curves. A generalized method for determining the parameters of the bilinear softening model was proposed and validated by the test results. Additionally, the fracture performance and crack extension of CEMI specimens were deeply analyzed using the double-K fracture criterion. The fracture initiation toughness K_{IC}^{ini} was calculated by introducing the cohesive fracture toughness, and the crack extension resistance K_R curves of the CEMI specimens were calculated by combining the linear-elastic fracture mechanics and the proposed bilinear softening model. It was indicated that the initiation locations and extension paths of interfacial cracks could be effectively identified by the DIC technique, with an error of less than 8% between test results and predictions. The bridging effect was strengthened by pre-coating with an epoxy solution of the CEMI specimens by filling the microscopic defects on the concrete surface, thereby improving K_{IC}^{ini}, delaying unstable crack extension, and enhancing interfacial fracture resistance.

Keywords: concrete-epoxy mortar interface; fracture performance; bilinear softening model; double K fracture criterion; cohesive fracture toughness

Check for updates

Academic Editor: Alessandra Mobili

Received: 19 May 2026
Revised: 15 June 2026
Accepted: 19 June 2026
Published: 21 June 2026

Copyright: © 2026 by the authors. Licensee MDPI, Basel, Switzerland. This article is an open access article distributed under the terms and conditions of the Creative Commons Attribution (CC BY) license.

1. Introduction

Due to the superior bonding strength, corrosion resistance, and aging durability, epoxy mortar has been extensively employed in the repair of concrete and composite structural connections. Compared to traditional cement-based bonding materials, epoxy mortar is particularly suitable for lifeline engineering, such as bridge engineering and road-paving engineering [1]. In composite structures, epoxy mortar is not only used as an adhesive, but stress transfer is also effectively facilitated by it, whereby stress concentration at interfaces is reduced, and overall structural stability is improved [2,3]. However, due to the low tensile strength and surface defects of concrete, the concrete-epoxy interface is easily cracked, especially under long-term loading. The cracking could be further developed

and propagated, by which the structural integrity is likely destroyed [4,5]. Therefore, it is critically important to investigate the fracture performance of the concrete-epoxy interface to enhance cracking resistance and ensure the long-term durability of composite structures.

Although a great deal of work has been completed toward improving the bonding performance of the concrete-epoxy mortar interface (CEMI), most efforts have been focused on bonding performance, material modification, and treatment of the CEMI. Understanding the fracture mechanisms and microscopic failure modes of the CEMI is still limited. As reviewed by Daneshvar et al. [6], the bond strength and fracture performance of the concrete-concrete interface (CCI) are highly influenced by design and environmental factors, and strategies to optimize interlayer bonding were further proposed. Li et al. [7] found that the bonding strength of the CCI was reduced by lower temperature, increased surface roughness, and higher humidity. Zhou et al. [8] and Jeong et al. [9] pointed out that the fracture toughness of the CCI can be reduced by the combined effects of humidity under sustained loading and high-temperature loading. The studies by Lee et al. [10] and Liang et al. [11] revealed that the degradation of bonding strength in the CCI was accelerated by the combination of cyclic wet-dry, thermal conditions, and sustained loading.

Yu et al. [12] reported that the load-bearing capacity and stiffness of the CEMI were reduced by excessively increasing the bonding layer thickness, while superior fracture toughness and load-bearing performance were provided by an optimal thickness of 5.0 mm. Hang et al. [4] found that the load-bearing capacity, crack initiation toughness, and crack propagation resistance of the CEMI can be greatly enhanced by increasing both the compressive strength of concrete and interfacial roughness. Ren et al. [13] observed that enhancing interfacial roughness resulted in improvements in bonding strength and failure modes. Zhao et al. [14] utilized an epoxy resin-acetone solution to pretreat the concrete surface to repair surface defects of the CEMI. Experimental results indicated that the deformation capacity and fracture performance of the CEMI were enhanced by the pre-coating. Similarly, Hang et al. [5] found that the interfacial bonding performance between epoxy mortar and concrete was enhanced by pre-coating treatment using epoxy resin, due to the improvement of the defects on the surface of the CEMI. Regarding material modification, Bahraq et al. [15] and Luo et al. [16] explored the application of graphene materials at the cement-epoxy interface. Of interest is the fact that bonding energy can be increased and the diffusion of moisture and chloride ions can be inhibited by nanomaterials. Furthermore, Zhang et al. [17] and Wang et al. [18] investigated the debonding failure mechanisms at the FRP-concrete interface using mesoscopic finite element models. It was observed that the performance of the FRP-concrete interface can be effectively enhanced by optimizing aggregate size and bonding layer thickness.

Numerous studies have been conducted to investigate the fracture behavior of quasi-brittle materials, such as concrete, composite materials, wood, and rock. Bilinear softening models, cohesive zone models, and the double-K fracture criterion have been explored to deeply investigate fracture toughness, cracking propagation characteristics, and mechanical behavior. Lou and Ma [19] investigated the cracking resistance of steam-cured concrete. It was found that when the temperature of the steam reached 45 °C, the K_R-curves and fracture toughness were maximized. Wang et al. [20] proposed a meso-scale model using a bilinear softening model to study the effects of porosity, aggregate strength, and volume fraction on the fracture performance of lightweight aggregate concrete. Yin et al. [21] proposed expressions to estimate the K_R-curves of three-point bending beams. The results indicated that the KR curves were not influenced by the span-to-height ratio; however, the K_R curves were significantly affected by the sectional height of the specimen. Furthermore, Yin et al. [22,23] used digital image correlation (DIC) to study the fracture performance of three-point bending beams with small span-depth ratios. Interestingly, it was observed

that the unstable toughness and the length of the fracture process zone were affected by changes in sectional depth; however, the K_R-curves were minimally affected by strain rates. Moreover, the critical cracking length was observed to increase linearly when the initial and unstable fracture toughness remained constant. A linear interpolation method for calculating fracture parameters was also proposed and validated. Guan et al. [24] employed the double-K fracture model to analyze the influences of porosity and micropore diameter on the fracture behavior of hematite concrete.

Yuan et al. and Liu et al. [25,26] employed bilinear softening curves and cohesive zone models to investigate crack propagation and fracture processes in concrete-rock composite interfaces and FRP composite materials. Moreover, Yuan et al. [27] assessed the impact of interface roughness on fracture toughness based on the double-K fracture criterion. Biswal et al. [28], Cintra et al. [29], and Yan et al. [30] employed cohesive zone models to study the I-type and II-type fracture behavior of pultruded glass fiber-polymer composites; furthermore, the fiber bridging mechanisms during crack propagation were described. Yu et al. [31] described the quasi-brittle fracture behavior of wood using bilinear softening models. The fracture properties were further studied through both the K_R and G_R resistance curves. Xu et al. [32] and Wu et al. [33] conducted a wide-ranging project aimed at analyzing crack propagation and fracture toughness in rocks using the double-K fracture model and K_R resistance curves. It was found that the fracture behavior of rock materials was significantly influenced by notch width, sharpness, and loading mode.

The fracture behavior of Type I cracks at the CEMI was investigated through four-point bending tests on nine specimens. First, combining DIC technology and SEM micro-analysis, the Mode-I crack-initiation load, crack-propagation process, and fracture energy dissipation of the interface were analyzed from both macroscopic and microscopic perspectives. Second, a simplified parameter determination method based on the tri-linear stiffness model was proposed to describe the constitutive behavior of the cohesive fracture zone. Finally, by combining the bilinear softening model with linear elastic fracture mechanics, the crack initiation toughness, unstable toughness and the K_R resistance curve for the interfacial crack were determined.

2. Experimental Program and Result Discussions of Four-Point Bending Tests

2.1. Design of Specimens

According to the epoxy solution concentrations and the fracture-mechanics-based specimen design recommendations provided in The Stress Analysis of Cracks Handbook [34], three sets of CEMI specimens (PB0%, PB20%, and PB40%) with three specimens each were designed. The test dimensions are depicted in Figure 1a. A total specimen size of 600 mm × 100 mm × 100 mm ($l \times b \times h$) was selected based on the testing apparatus and prior experience. To ensure pure bending and stable crack initiation, the span-to-height ratio d_1/h = 4.0 and the notch-to-depth ratio a_0/h = 0.2 were adopted. Moreover, the thickness t_e of the epoxy mortar was selected to 2.4 mm, reflecting both typical engineering practice and the actual measured specimen dimensions. As shown, the distance d_1 between the two bottom simply supports was set to 400 mm, leading to d_1/h equaling 4.0, while the distance d_2 between the upper two loading points was set to 100 mm.

As illustrated in Figure 1b, the flaws on the surface of the concrete block were first repaired using the epoxy solution, and then two identical concrete blocks were connected by epoxy mortar. First, the concrete surface was cleaned with ethanol, and then foam adhesive was applied to the surface to control the thickness of the incision and epoxy mortar. Subsequently, the acetone and epoxy solutions were mixed in a preset ratio to form a pre-coating solution, which was uniformly applied to the concrete surface. The

prepared epoxy mortar was uniformly applied to each concrete surface before the pre-coating solution was completely dry. The concrete block without foam adhesive was then rotated 180 degrees and stacked on top of another concrete block to form a composite specimen, which was manually vibrated for 15 min and continued to cure for 7 days. After curing, the area of interest (AOI), shown in Figure 1b on the surface of the specimen, was sanded and cleaned. Finally, white matte paint was sprayed on the AOI area, followed by random and uniform spraying of black ink to obtain a high-quality scattering pattern.

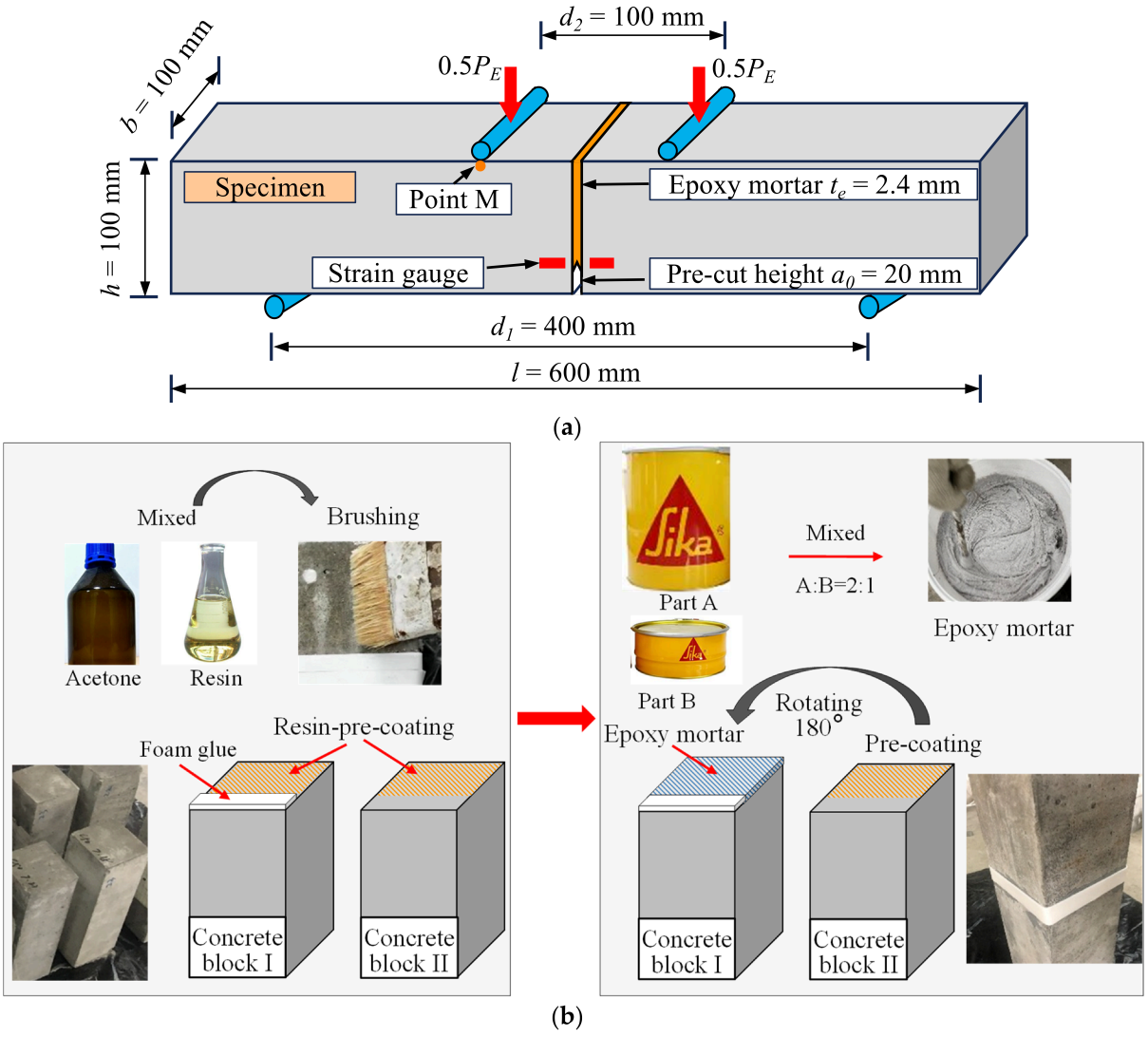


Figure 1. Design of specimen: (**a**) Dimension; (**b**) Preparation.

2.2. Materials

The specimens were composed of three types of materials: concrete, epoxy mortar and pre-coating solution. Concrete was prepared following the GB50010-2010. "Code for the Design of Concrete Structures" [35], with a ratio of cement: fly ash: powder: sand: aggregate: water: chemical admixture = 1: 0.33: 0.33: 2.71: 3.73: 0.56: 0.02, as shown in Table 1. After preparation, the specimens were prepared according to the GB/T 50081-2002 "Test Methods for Mechanical Properties of Ordinary Concrete" [36]. A total of 30 concrete cube specimens with dimensions of 150 mm × 150 mm × 150 mm were fabricated, all of which were cured in a steam condition for 28 days. The mechanical properties of the concrete were tested on the 28th day according to the Chinese standard GB/T 50081-

2002 [36], and the results showed that the compressive strength, tensile strength, and elastic modulus of the concrete were measured as 56.84 MPa, 4.01 MPa, and 35.34 GPa, respectively.

Table 1. Mixture ratio of concrete (kg/m^3).

Series	Cement	FA	Ore Fines	Sand	CA	Water	Additive	W/B	f_c (MPa)	f_t (MPa)	E_c (GPa)
C50	283	94	94	766	1057	146	4.71	0.32	56.84	4.01	35.34

The epoxy mortar material was Sikadur®-31 CF Normal epoxy resin mortar provided by Sika Co., a local Chinese company. It was composed of two components: component A and component B. Component A was mainly composed of bisphenol A-based epoxy resin and aggregate, etc., while component B was a curing agent containing benzyl alcohol, hydrocarbons, and trimethylcyclohexylamine, as shown in Table 2. The epoxy mortar was mixed at a mass ratio of 2:1 (component A: component B). The material property tests of the epoxy mortar were conducted according to "DL/T5193-2004 Technical Specification for Epoxy Resin Mortar" [37]. The test results showed that the compressive strength, tensile strength, and elastic modulus of the epoxy mortar were measured as 63.14 MPa, 14.18 MPa, and 1.31 GPa, respectively.

Table 2. The main mixing properties of epoxy mortar.

Composition	Components	Concentration (%)	f_c (MPa)	f_t (MPa)	E_c (GPa)
Component A	Reaction product: Bisphenol-A-(epichlorhydrin), epoxy resin	20~25	63.14	14.18	1.31
	Oxirane, mono[(C12-14-alkyloxy)methyl] derives	1~10			
	Hydrocarbons, C10–C13, aromatic, >1% Naphthalene	1~2.5			
	Naphthalene	0.1~0.25			
Component B	Benzyl alcohol	1~10			
	3-aminomethyl-3,5,5-trimethylcyclohexylamine	3~5			
	3,6-diazaoctannethylenediamin	3~5			
	Hydrocarbons, C10–C13, aromatic, >1% Naphthalene	2.5~10			
	2,4,6-tris (dimethylaminomethyl) phenol	1~3			
	Reaction product of BADGE with IPDA and TMDA	1~2.5			
	Naphthalene	0.25~1			

The pre-coating solution was made by mixing epoxy resin and acetone. The adhesion between the mortar and the concrete was enhanced by the epoxy resin, which was utilized for its excellent adhesion and chemical resistance. The viscosity of the epoxy resin was reduced by the acetone, which was used as a highly volatile diluent, allowing the pre-coating solution to easily penetrate and fill the defects on the concrete surface, and the curing process was accelerated. Two types of pre-coating solutions with epoxy resin concentrations of 20% and 40% were prepared by acetone dilution. However, due to the fast volatilization of acetone, the pre-coating solution needed to be uniformly brushed onto the concrete surface immediately after preparation. Furthermore, the assembly of the CEMI specimens was required to be rapidly completed before the pre-coating solution dried.

2.3. Test Setup

The test setup of the four-point bending test is shown in Figure 2, and the test was conducted at Shantou University, China. A 20-kN compressive test machine was used to press the test specimen, with displacement control employed, and the loading speed was 0.5 mm/min. A 10-kN load cell was used to record the axial load and displacement data. Strain gauges were attached to the two sides of the tip of the pre-cut (as shown in Figure 1). Electrical resistance strain gauges (BA120-3AA, 120 Ω resistance, 3 mm gauge length, and sensitivity coefficient of 2.08 ± 1%) were used in this study. Before installation, the concrete surface near the pre-cut tip was mechanically polished to remove the laitance layer, cleaned with anhydrous ethanol, and then thoroughly dried. The strain gauges were bonded using cyanoacrylate adhesive (502), carefully positioned, and pressed firmly for at least 30 s to ensure full contact and a void-free bonding interface. After curing of the adhesive, a stable strain-transfer interface was formed between the strain gauges and the concrete surface. The total weight of the test specimen, distribution beam, simply supports, and load cell together was measured as 25.73kg.

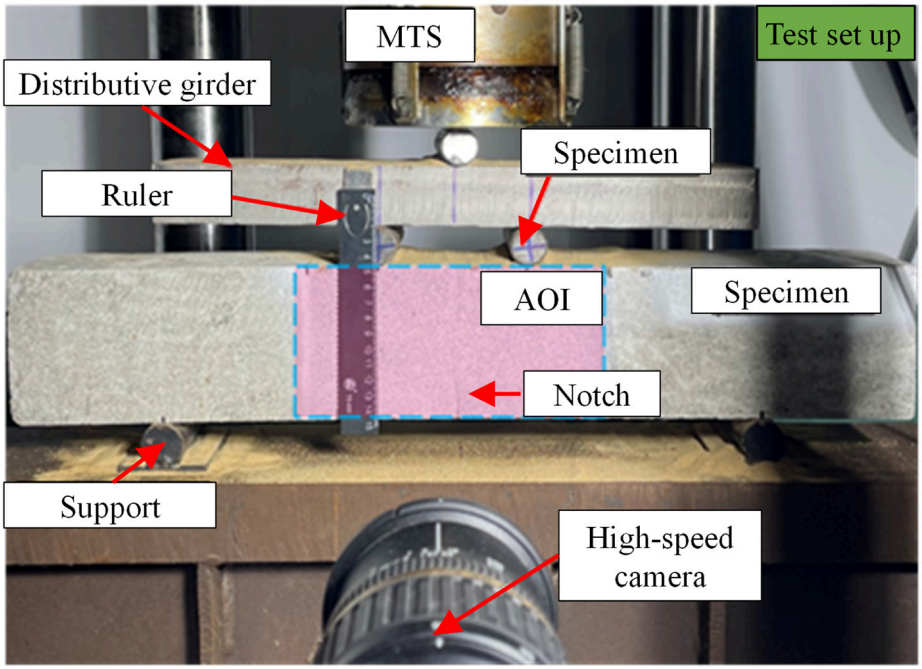


Figure 2. Test setup.

The DIC has been extensively used in civil engineering due to its high division rate and full-area strain measurement [38,39]. The DIC system was used to measure the stress and displacement fields of the AOI area of CEMI specimens, crack tip opening displacement (*CTOD*) at the tip of the pre-cut, equivalent cracking length under the maximum loading a_c, deflection at the middle span D, and the axial deflection at the loading point D_M (as shown at the M point in Figure 1). Two high-speed cameras were placed in front of the test specimen; the first one was used to record the entire testing process at a speed of 33 frames per second, and the other one was used to capture images of failure within 5 s at a speed of 400 frames per second. The images were acquired at a resolution of 1600 × 1200 pixels, with each pixel size of 0.062 mm, and the total system resolution was determined to be 0.01 mm, yielding a DIC metrology accuracy of 0.62 μm. DIC data were processed using VIC-2D (Correlated Solutions, Inc., Columbia, SC, USA.) with the following parameters: subset size 21 × 21 pixels, step size 5 pixels, and bi-cubic spline interpolation for sub-pixel accuracy. Strain fields were calculated using a 15 × 15 data point window. The analysis

procedure was divided into four steps: (1) speckle pattern preparation on the AOI; (2) image acquisition using two high-speed cameras; (3) displacement and strain field calculation; and (4) extraction of *CTOD*, *CMOD*, and deflection by tracking feature points.

2.4. Test Results

Two types of methods were used to determine the initiation load of the test specimens. The first method was based on the P_E-ε curves of the test specimens shown in Figure 3, with the strain measured by the gages attached to the positions near the tip of the pre-cut shown in Figure 1. As depicted, the transition point from the maximum strain (as shown by the circle in Figure 3) was referred to as the initiated load P_{ini}'. The second method was determined by the DIC data [5], as illustrated in Figure 4. The initial loads of the test specimens obtained by the above two methods are provided in Table 3. As shown, the errors between P_{ini}' and P_{ini} were found to be very small, implying that the DIC could be effectively employed to estimate the fracture performances of CEMI specimens.

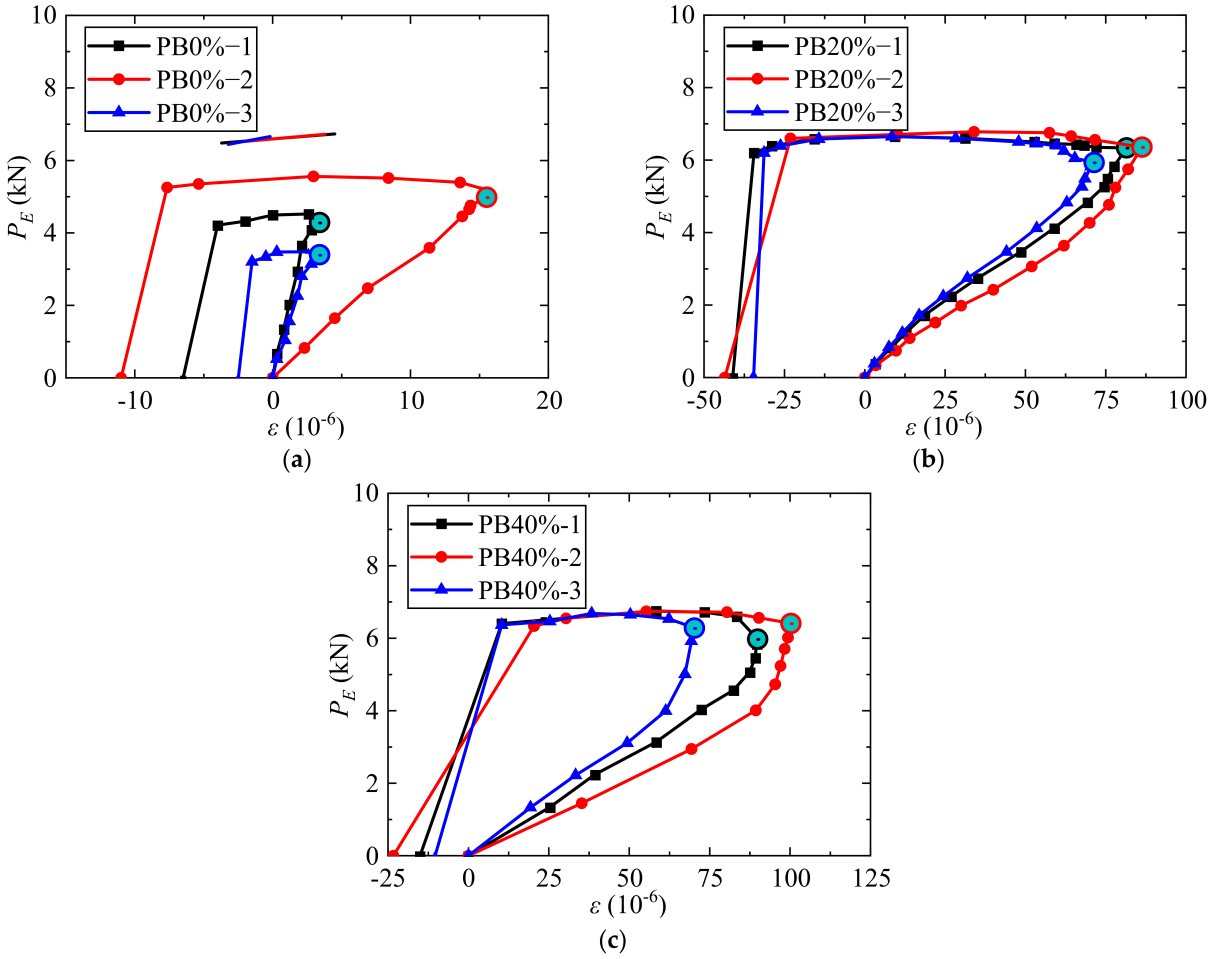
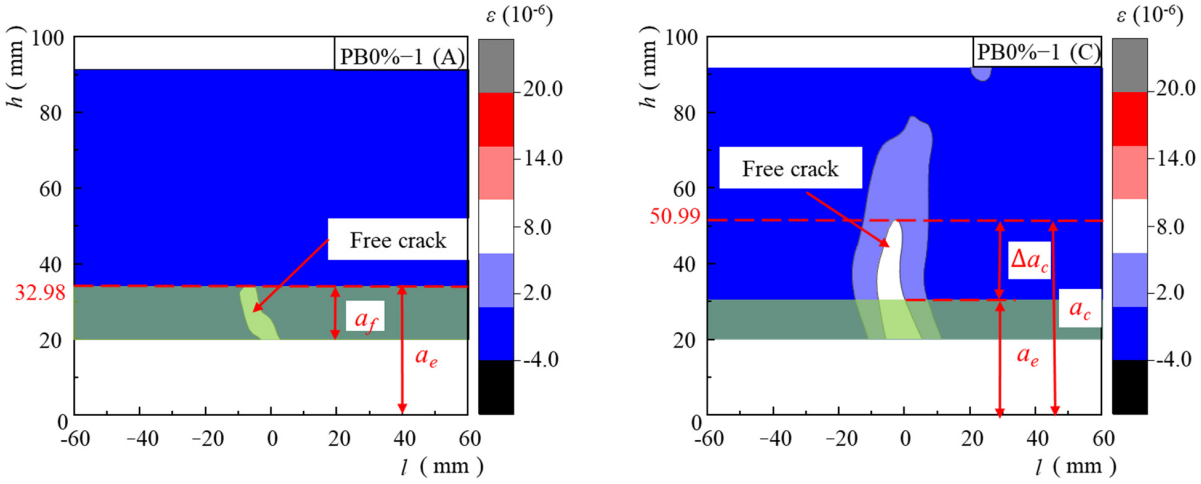


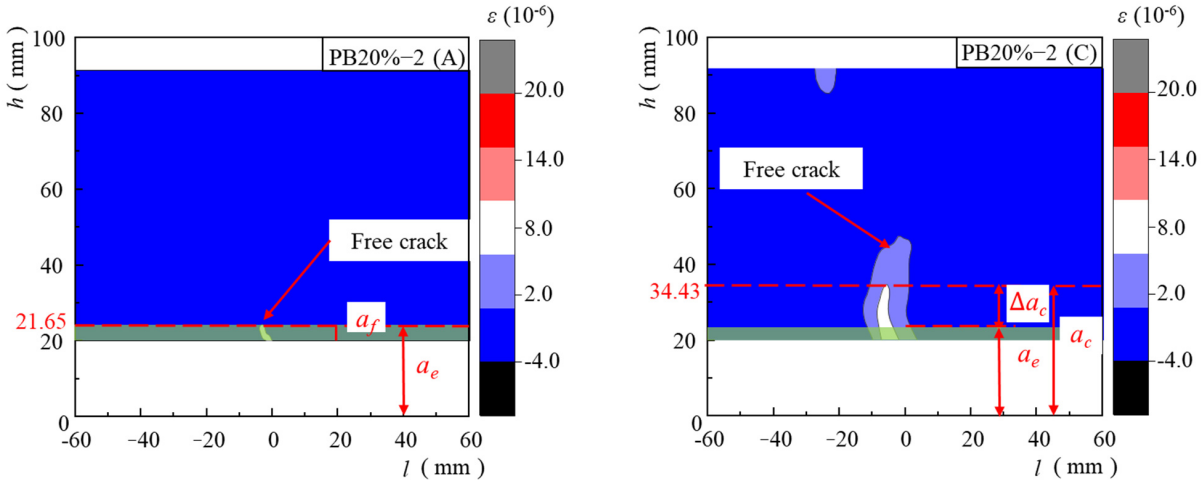
Figure 3. P_E-ε curves of specimens: (**a**) PB0% specimens; (**b**) PB20% specimens; (**c**) PB40% specimens.

The P_E-D, P_E-D_M, P_E-*CTOD*, and P_E-*CMOD* curves of the test CEMI specimens are presented in Figure 5. As indicated, an obvious I-type brittle fracture behavior is displayed by all test CEMI specimens. It is observed that the post-peak curves of the test CEMI specimens are characterized by linear behavior due to the difficulty in recording test data after instantaneous failure occurs. All curves essentially are composed of three stages: the elastic stage, representing no cracks; the plastic stage, representing the development of cracks; and the post-peak stage, representing the unstable development of cracks, as depicted in Figure 5e. Cracking initiation, peak loading, and failure are represented by

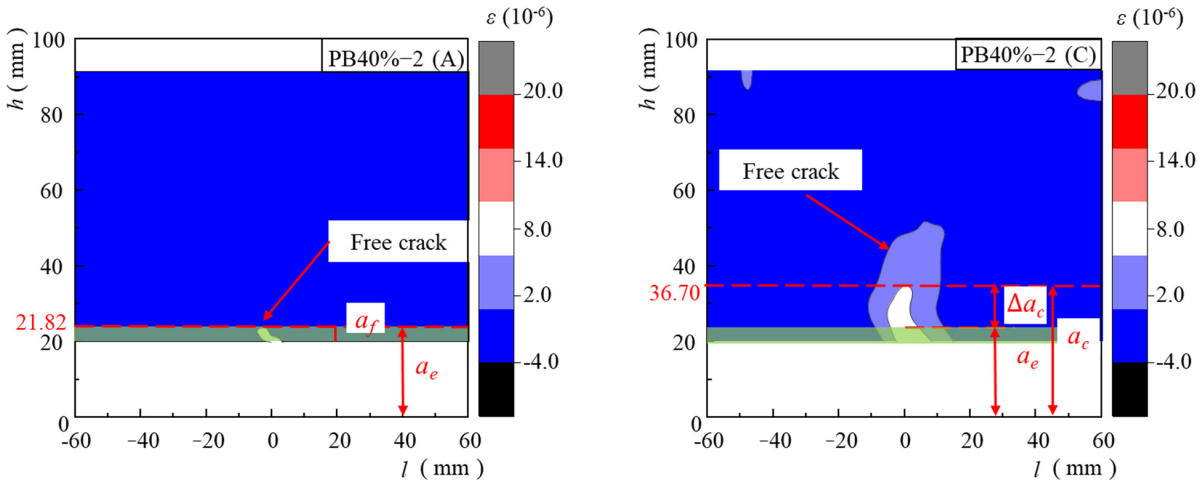
Points A, B, and C in Figure 5e, respectively. Moreover, the difference among the three specimens with the identical epoxy solution concentration was found to be smaller than that of the control normal specimens. As shown, the elastic stiffness of the test specimens PB20% and PB40% was found to be larger than that of the test specimens PB0%, and the largest elastic stiffness was exhibited by the test specimen PB20%.



(**a**)



(**b**)



(**c**)

Figure 4. Strain fields: (**a**) PB0% specimens; (**b**) PB20% specimens; (**c**) PB40% specimens.

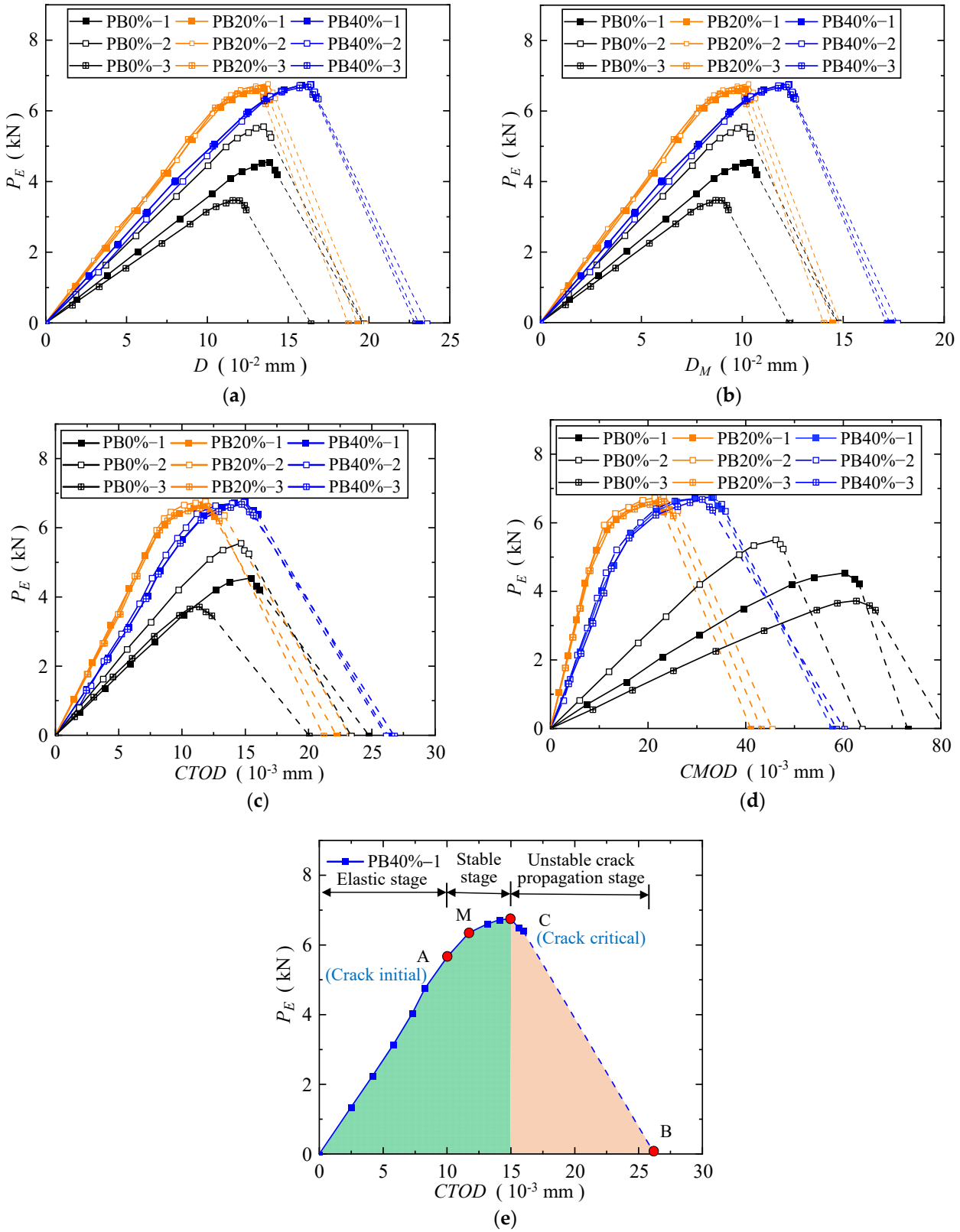


Figure 5. Applied load versus displacement curves of specimens: (**a**) P_E-D curves; (**b**) P_E-D_M curves; (**c**) P_E-*CTOD* curves; (**d**) P_E-*CMOD* curves; (**e**) Typical P_E-*CTOD* curve.

The main test results of test specimens, including the initiated load P_{ini}, maximum load P_{max}, the corresponding cracking lengths $\Delta a_A'$and $\Delta a_c'$, the cracking length at the failure point $\Delta a_B'$, and the crack tip opening displacement $CTOD_c$ and crack mouth opening displacement $CMOD_c$ under maximum load P_{max}, are displayed in Table 3. As indicated in

Figure 6 and Table 3, the average cracking initiation loads of PB20% and PB40% specimens were increased by 45.71% and 50.95%, respectively, compared to the control normal test specimens PB0%. Compared to the control PB0% specimens, the maximum loads of test specimens PB20% and PB40% were increased by 48.41% and 49.30%, respectively, while the corresponding *CTODcs* of them were increased by -12.49% and 9.01%, respectively. However, the *CMODcs* of the PB20% and PB40% specimens were decreased by 55.28% and 36.50%, respectively.

Table 3. Experimental results.

Specimen	P_{ini}' kN	P_{ini} kN	P_{max} kN	P_{ini}'/P_{ini}	a_e mm	$\Delta a_A'$ mm	$\Delta a_M'$ mm	$\Delta a_C'$ mm	$\Delta a_B'$ mm	$CTOD_c$ 10^{-3} mm	$CMOD_c$ 10^{-3} mm
PB0%-1	4.29	4.08	4.52	1.05	32.98	0	11.76	18.76	30.21	15.45	52.62
PB0%-2	4.99	5.23	5.51	0.95	26.13	0	12.36	16.36	33.11	14.92	39.95
PB0%-3	3.41	3.30	3.48	1.03	41.35	0	10.27	15.56	25.05	10.45	60.62
PB20%-1	6.31	6.32	6.63	1.00	20.12	0	10.19	13.21	38.85	11.63	22.12
PB20%-2	6.09	6.12	6.77	1.00	21.65	0	9.61	12.69	37.86	12.13	23.14
PB20%-3	5.93	5.91	6.65	1.00	22.16	0	9.63	12.72	39.95	11.96	23.25
PB40%-1	6.28	6.31	6.75	1.00	21.22	0	10.98	13.90	38.44	14.97	32.91
PB40%-2	6.41	6.43	6.74	1.00	21.82	0	11.83	14.88	36.24	14.85	33.32
PB40%-3	6.28	6.29	6.68	1.00	21.35	0	10.23	12.88	37.11	14.68	31.04

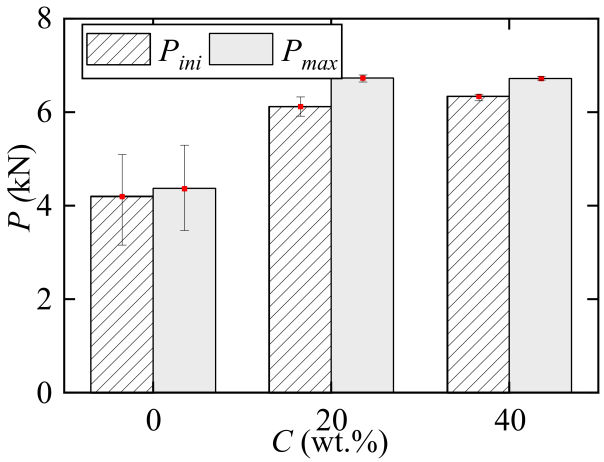


Figure 6. Comparison of the fracture properties of specimens.

As shown in Table 3, the PB20% and PB40% specimens exhibit high similarity in key mechanical properties, including P_{ini}, P_{max}, and *CTOD*. This phenomenon is primarily attributed to the saturation effect of the pre-coating treatment on the repair of surface micro-defects. Owing to the strong permeability of the acetone-based diluent, a 20% epoxy resin concentration is already sufficient for the micro-defects on the concrete surface to be fully penetrated and filled, forming a dense bridging structure. Beyond this threshold, no significant benefit is provided by further increasing the concentration to penetration and filling.

The typical failure modes of representative test specimens are presented in Figure 7. As shown in Figure 7a, for the PB0% specimen without pre-coating of the epoxy solution, only a small amount of concrete spalling was observed at the interface, accompanied by distinct bond damage. It is further revealed by SEM images that numerous micro-cracks and open pores with an uneven distribution were observed on the fracture surface. This suggests that the micro-defects on the concrete surface were not adequately penetrated by the epoxy mortar, leading to the formation of local voids and a limited number of effective

bridging structures. Under external loading, these voids were prone to coalesce, by which stress-free cracks that cannot effectively transfer loads were formed.

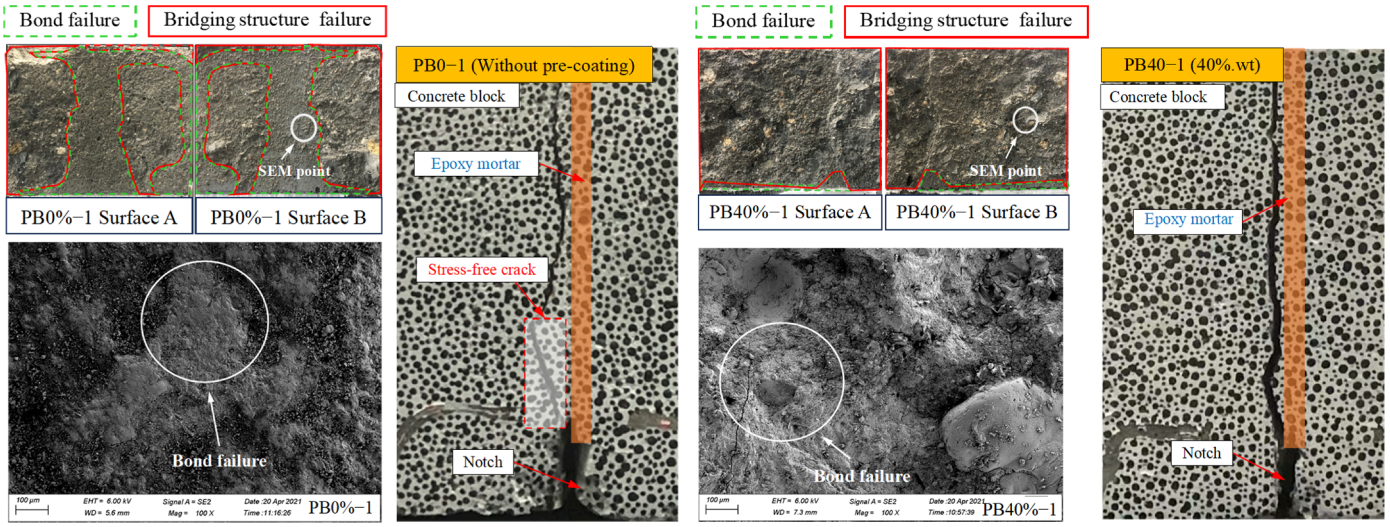


Figure 7. Typical failure mode of interface: (**a**) PB0%−1 specimen; (**b**) PB40%−1 specimen.

In contrast, for the PB40% specimens with pre-coating, obvious cracking on the concrete surface and extensive concrete spalling were observed, as depicted in Figure 7b. A typical cohesive failure mode within the concrete was observed, where cracks were propagated through the concrete matrix and characteristic features of bridging structure failure were exhibited by the fracture surface. As confirmed by SEM images, the surface defects of the PB40% specimen were found to be significantly smaller than those of the PB0% specimen. This difference can be attributed to the distinct penetration capabilities of the two treatment methods. While the epoxy mortar can only fill larger pores, the liquid epoxy solution can more effectively fill the micro-pores to form a more efficient bridge link between the concrete and the epoxy mortar. Consequently, the fracture resistance of the CEMI specimens with pre-coating was significantly enhanced by these bridge links.

3. Constitute the Relationship of CEMI

3.1. Proposed Bilinear Softening Model

A bilinear softening model is proposed to investigate the I-type fracture characteristics of CEMIs pretreated by the epoxy solution. It is assumed that a virtual crack transmits normal positive stress to equivalently characterize the I-type fracture behavior. The fracture initiation of the CEMI is directly related to the toughening effect of the pre-coating and the tensile strength of concrete, f_t [5,14]. A toughening factor α is introduced, and eventually, αf_t is used as the equivalent tensile strength f_t' of the CEMI.

The proposed bilinear model is depicted in Figure 8, and the equation is given in Equation (1). It should be noted that the meanings of Points A, B, and C are identical to those of the same points shown in Figure 5e. As illustrated, when the equivalent cracking cohesive stress σ reaches the equivalent tensile strength f_t'(as shown at Point A), the equivalent crack in the cohesion area of CEMI is initiated. With the further extension of the equivalent crack, the crack tip opening displacement $CTOD(w)$ is gradually increased. When the σ is gradually decreased to 0, the $CTOD$ reaches the ultimate w_0 (as shown at Point B), representing the equivalent crack fully opening. As depicted in Figure 8, a critical

value of the crack tip opening displacement w_c and cohesive stress σ_c is represented by Point C [40,41].

$$\sigma = \begin{cases} f_t' - (f_t' - \sigma_c)w/w_c & 0 \le w < w_c \\ \sigma_c(w_0 - w)/(w_0 - w_c) & w_c \le w < w_0 \\ 0 & w = w_0 \end{cases} \quad (1)$$

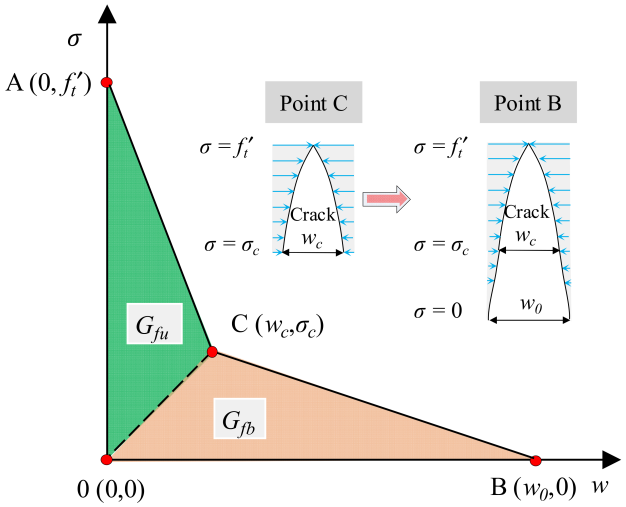


Figure 8. Bilinear model of tensile strength of concrete.

As shown in Figure 8, the fracture energy G_f of the CEMI is represented by the area under the curve, which is composed of the fracture energies due to the micro-cracks G_{fu} and bridge structures G_{fb}. Moreover, G_f, G_{fu}, and G_{fb} are determined by the calculations of the αf_t, σ_c, w_c, and w_0, as shown in Equations (2) and (3) [26]. The tensile strength of concrete f_t is obtained through tensile testing, and w_c and w_0 are measured using DIC in this study. However, the coefficients of α and σ_c are difficult to directly measure during testing. Consequently, it is important to determine G_{fu} and G_{fb} in order to calculate both α and σ_c.

$$G_{fu} = \int_0^{w_c} f_t'(1 - w/w_c)dw = 0.5\alpha f_t w_c \quad (2)$$

$$G_{fb} = \int_0^{w_c} (w\sigma_c/w_c)dw + \int_{w_c}^{w_0} \sigma_c(w_0 - w)/(w_0 - w_c)dw = 0.5\sigma_c w_0 \quad (3)$$

3.2. Calculation of Fracture Energy

The fracture energy calculation from the load–displacement curves is shown in Figure 9, and the definitions of points A, B, and C in the figure are the same as those in Figure 8. Moreover, the total load and vertical deflection under the loading point are denoted by P and D_M, respectively; The vertical deflection under the loading point when the external load P_E is 0 is denoted by D_0; and the vertical deflection under the loading point at failure is denoted by D_{max}. As shown in Figure 9a, the effect of the self-weights of the specimen (P_G) and the distributing beam (P_E) should be considered in the calculation. Therefore, the total load P can be calculated according to Equation (4).

$$P = P_E + P_G \quad (4)$$

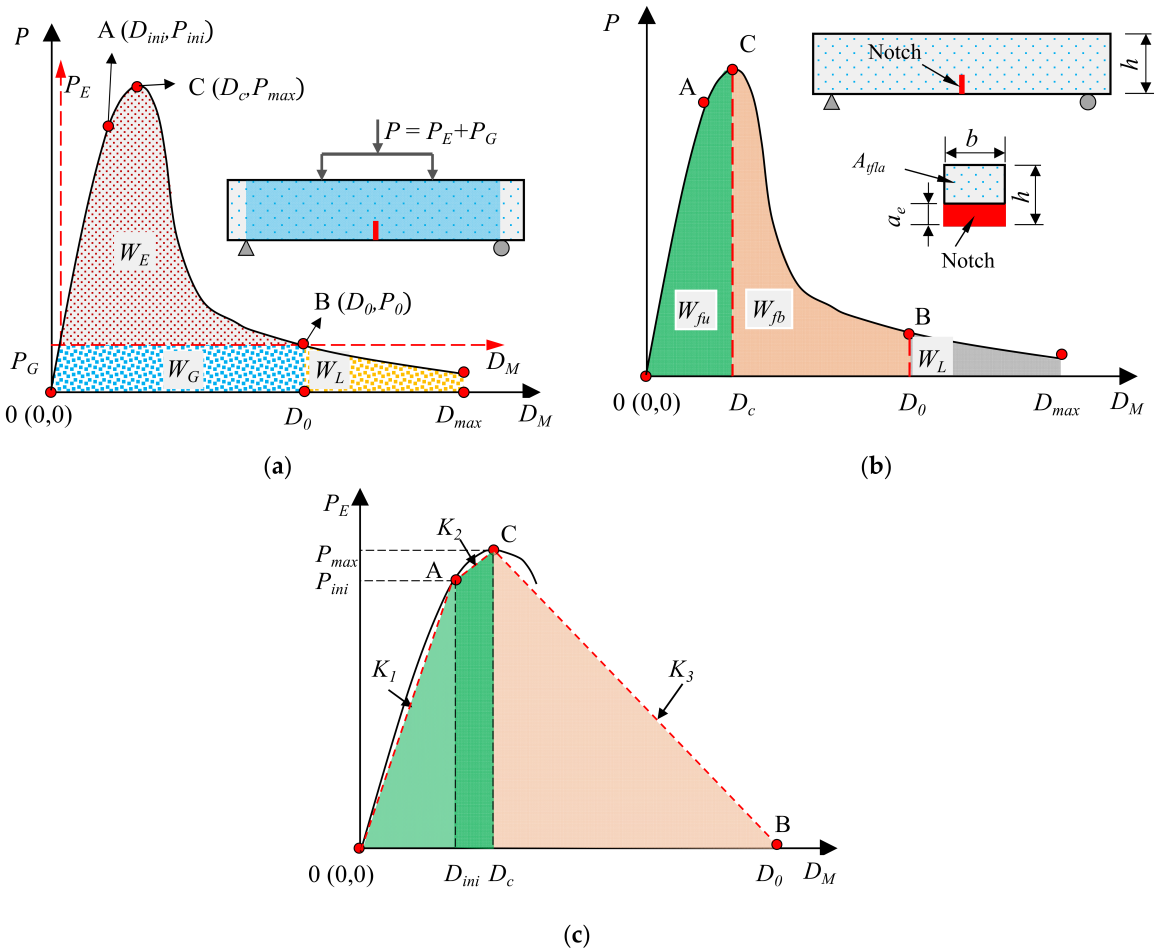


Figure 9. Analysis of fracture energy: (**a**) the work done by external forces; (**b**) the fracture energy of the specimen; (**c**) the triple-fold stiffness model.

The area W_T enclosed by the total load–displacement curve $f(D_M)$ shown in Figure 9a, i.e., the total work done by the external force on the specimen, can be calculated according to Equation (5).

$$W_T = \int_0^{D_{max}} f(D_M) d_{D_M} = W_E + W_G + W_L \tag{5}$$

Mehrab et al. [42] and Swartz et al. [43] proposed that the work done by the self-weight of the specimen (W_G) is equal to the work done by the loading (W_L), and that D_{max} equals $2D_0$, based on both experimental and theoretical results. Therefore, as shown in Figure 9a, $W_G = P_G \times D_0$. The total work W_T is given by the external force on the specimen and can be calculated according to Equation (6).

$$W_T = \int_0^{D_0} f(D_M) d_{D_M} + 2P_G D_0 \tag{6}$$

It is assumed that the total work W_T done by the external force on the specimen is used for the development of cracks in the fracture zone of the CEMI. The fracture energy per unit area of the specimen at failure, G_f', can be calculated according to Equation (7). Moreover, G_f' can also be calculated by Equation (8) [4].

$$G_f' = W_T / A_{tfla} \tag{7}$$

$$G_f' = (W_E + mgD_{max}) / A_{tfla} \tag{8}$$

In Equations (7) and (8), the nominal fracture area is denoted by A_{tfla}, which can be calculated according to Equation (9). The total mass of the specimen and the distributing beam is denoted by m, and the acceleration of gravity is denoted by g, taken as 9.8 N/kg.

$$A_{tfla} = b(h - a_e) \tag{9}$$

According to Equations (5) to (8), it can be obtained that $P_G\ D_0 = 0.5mgD_{max}$. When the vertical deflection D_M is equal to D_0, the fracture energy G_f can be calculated according to Equation (10).

$$G_f = (W_E + mgD_0)/A_{tfla} \tag{10}$$

As shown in Figure 9b, W_T can be calculated according to Equation (11) by drawing vertical dashed lines at points C and B. The area enclosed by the curve and the coordinate axis is divided into three parts: the work W_{fu} done by the external force due to microcrack extension, the work W_{fb} done by the external force of the bridge structure at the crack, and the work W_L done by P_G when the vertical deflection is increased from D_0 to the maximum deflection D_{max}. The microcrack rupture energy G_{fu} and the fracture energy of the bridge structure at the crack G_{fb} can eventually be calculated according to Equations (11) and (12).

$$G_{fu} = \left[\int_0^{D_c} f(D_M)d_{D_M} + mgD_c\right]/A_{tfla} \tag{11}$$

$$G_{fb} = \left[\int_{D_c}^{D_0} f(D_M)d_{D_M} + mg(D_0 - D_c)\right]/A_{tfla} \tag{12}$$

To simplify the calculation, the load-deflection curve is divided into three stages: elasticity, stable extension and unstable extension, as described in Figure 5e. W_{fu} can be subdivided into W_{fu1} and W_{fu2}, which represent the work done by the external force caused by the microcrack extension in the elastic and stable extension stages, respectively. The work done by the external forces at different stages is represented by the equivalent stiffness K and the maximum load P_{max}.

The triple-fold model is depicted in Figure 9c. As indicated, the vertical deflection when the initiating load P_{ini}, maximum load P_{max}, and external load P_E reach 0 are denoted by D_{ini}, D_c, and D_0, respectively. These values could be directly obtained from the measurements during testing. Consequently, the stiffness of the elastic stage is expressed as $K_1 = P_{ini}/D_{ini}$, the stiffness of the stable extension stage is expressed as $K_2 = (P_{max} - P_{ini})/(D_c - D_{ini})$, and the stiffness of the instability stage is expressed as $K_3 = P_{max}/(D_0 - D_c)$.

Particularly, the initiation load P_{ini} is defined according to the ratio β of the initiation load to the maximum load, $P_{ini} = \beta P_{max}$. By analyzing the test data in this paper and those of similar specimens in the literature [4], it was found that the β for the CEMI specimen in the four-point bending test was stable in the range of 0.88–0.95. For simplicity, an average value of 0.92 was used for β. Finally, the G_{fu1} and G_{fu2} in the elastic and stable extension stages, and the bridging-structure fracture energy G_{fb}, can be calculated according to Equations (13)–(16).

$$G_{fu1} = \frac{\beta P_{max}(\beta P_{max} + 2mg)}{2K_1 A_{tfla}} \tag{13}$$

$$G_{fu2} = \frac{[(1+\beta)P_{max} + 2mg](1-\beta)P_{max}}{2K_2 A_{tfla}} \tag{14}$$

$$G_{fu} = G_{fu1} + G_{fu2} = \frac{P_{max}^2[\beta^2(K_2 - K_1) + K_1] + 2mgP_{max}[\beta(K_2 - K_1) + K_1]}{2K_1 K_2 A_{tfla}} \tag{15}$$

$$G_{fb} = \frac{(P_{max} + 2mg)P_{max}}{2K_3 A_{tfla}} \tag{16}$$

The calculated results of fracture energy for each specimen are listed in Table 4, including the fracture energies G_f', G_{fu}', and G_{fb}' obtained by integrating the load–displacement curves, and the fracture energies G_f, G_{fu}, and G_{fb} based on the triple-folding model using the equivalent stiffnesses and maximum loads. As depicted in Table 4, the maximum error between the results of the two methods is 13.0%, indicating that the triple-folding model provides good accuracy in assessing the fracture energy of pre-coated CEMI specimens.

Table 4. Calculated results of fracture energy.

Specimen	G_f' J/m^2	G_{fu}' J/m^2	G_{fb}' J/m^2	K_1 kN/mm	K_2 kN/mm	K_3 kN/mm	G_f J/m^2	G_{fu} J/m^2	G_{fb} J/m^2	G_f'/G_f	G_{fu}'/G_{fu}	G_{fb}'/G_{fb}
PB0%-1	43.96	31.49	12.46	47.60	30.80	96.10	42.36	29.07	13.29	1.04	1.08	0.94
PB0%-2	53.88	33.67	20.11	58.96	40.23	107.00	52.22	34.48	17.73	1.03	0.98	1.13
PB0%-3	28.32	19.64	8.68	40.82	31.87	95.99	27.27	19.38	7.89	1.04	1.01	1.10
PB20%-1	65.36	47.27	18.09	70.59	26.35	153.44	66.85	48.95	17.90	0.98	0.97	1.01
PB20%-2	69.25	49.78	19.48	76.63	28.17	149.36	66.44	47.26	19.18	1.04	1.05	1.02
PB20%-3	63.59	45.85	17.74	76.23	28.05	157.46	63.42	45.84	17.58	1.00	1.00	1.00
PB40%-1	80.83	59.60	21.23	61.75	21.38	134.32	80.69	59.49	21.20	1.00	1.00	1.00
PB40%-2	80.60	58.54	22.06	61.06	17.97	128.45	85.85	63.75	22.10	0.94	0.92	1.00
PB40%-3	79.72	58.42	21.30	61.57	20.14	134.23	80.15	59.38	20.78	0.99	0.98	1.03

The comparisons of the calculated fracture energy of the CEMI specimens are illustrated in Figure 10. From the figure, it was observed that the fracture energy $G_f's$ of the PB20% and PB40% specimens were improved by 57.1% and 91.2%, respectively, compared to the control normal PB0% specimens. This indicates that the fracture resistance of the CEMI specimen is significantly enhanced by the pre-coating using epoxy solution.

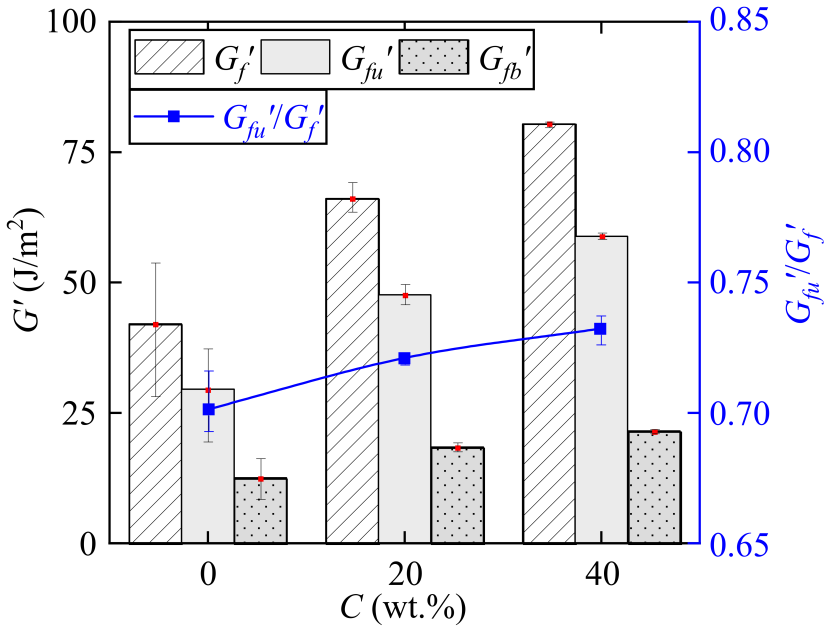


Figure 10. Calculated fracture energy.

3.3. Determination of the Coefficients of the Bilinear Softening Model

As previously stated, the surface micro-defects are filled by the pre-coating using epoxy solution, by which numerous "bridge structures" are generated in the CEMI. As illustrated in Figure 7, the fracture resistance of the CEMI specimens with pre-coating was significantly improved. To quantify the improvement due to the pre-coating, an enhanced factor α was introduced [5,14]. The factor α was calculated by substituting Equation (2) into

Equation (11) to obtain Equation (17), and the results are shown in Table 5. It is assumed that the factor α of the normal PB0% specimen is approximately 1.0. As indicated, the αs for both PB20% and PB40% specimens were found to be approximately 2.0.

Table 5. Calculated results of softening curves.

Specimen	G_f J/m^2	G_{fu} J/m^2	G_{fb} J/m^2	α	K_1 kN/mm	K_2 kN/mm	K_3 kN/mm	σ_c MPa	w_c 10^{-3} mm	$CTOD_c$ 10^{-3} mm	W_c /$CTOD_c$
PB0%-1	42.36	29.07	13.29	1.02	47.60	30.80	96.10	1.01	14.50	15.45	0.94
PB0%-2	52.22	34.48	17.73	1.10	58.96	40.23	107.00	1.13	17.20	14.92	1.15
PB0%-3	27.27	19.38	7.89	0.86	40.82	31.87	95.99	0.90	9.66	10.45	0.92
PB20%-1	66.85	48.95	17.90	2.01	70.59	26.35	153.44	1.61	12.22	11.63	1.05
PB20%-2	66.44	47.26	19.18	2.04	76.63	28.17	149.36	1.79	11.79	12.13	0.97
PB20%-3	63.42	45.84	17.58	1.99	76.23	28.05	157.46	1.68	11.42	11.96	0.95
PB40%-1	80.69	59.49	21.20	1.99	61.75	21.38	134.32	1.57	14.84	14.97	0.99
PB40%-2	85.85	63.75	22.10	1.98	61.06	17.97	128.45	1.58	15.90	14.85	1.07
PB40%-3	80.15	59.38	20.78	1.99	61.57	20.14	134.23	1.54	14.81	14.68	1.01

The critical cohesive stress σ_c was calculated by substituting Equation (3) into Equation (12) to obtain Equation (18), and the results are shown in Table 5. The σ_c values for the PB20% and PB40% specimens were increased by 68% and 53%, respectively, compared with those of the normal PB0% specimen. This implies that the cohesion of the CEMI can be effectively improved by the pre-coating. However, it is indicated that too high a concentration of the epoxy solution is not beneficial for improving the cohesion.

$$\alpha = 2\left[\int_0^{D_c} f(D_M)d_{D_M} + mgD_c\right] / \left(f_t w_c A_{tfla}\right) \tag{17}$$

$$\sigma_c = 2\left[\int_{D_c}^{D_0} f(D_M)d_{D_M} + mg(D_0 - D_c)\right] / \left(w_0 A_{tfla}\right) \tag{18}$$

To simplify the derivation of the bilinear softening model for the CEMI, the triple-fold model shown in Equations (17) and (18) is adopted in this study. Additionally, the stiffness *K*s in the elastic phase, stable extension phase, and the unstable phase, as well as the maximum load P_{max}, are obtained based on the $P_E - D_M$ curves of the specimens shown in Figure 5, as presented in Equation (19).

To assure the accuracy and stability of the calculation, the parameters λ, β and α in Equation (19) are quantitatively analyzed based on the experimental data presented in this paper. First, λ is taken as 0.55 based on the observation of W_c/W_0 in the $P_E - CTOD$ curve shown in Figure 5. Second, the ratio β of the P_{ini} to P_{max} is assumed to be 0.92, based on the experimental data from this paper and the data from the literature [4]. Finally, as previously stated, α is assumed to be 2.0 for the PB20% and PB40% specimens and 1.0 for the normal PB0% specimen.

The calculated w_cs of the specimens according to Equation (19) are shown in Table 5. As observed, the error between the test results and the predicted results is approximately 8.09%, except for the PB0%− 2 specimen, which has an error of 15.25%. Consequently, Equation (19) could be used to predict the bilinear softening curves of the specimens with good accuracy.

$$\begin{cases} \sigma_c = \frac{\lambda K_1 K_2 \alpha f_t (P_{max}+2mg)}{K_3[[\beta^2(K_2-K_1)+K_1]P_{max}+2mg[\beta(K_2-K_1)+K_1]]} \\ w_c = \frac{P_{max}^2\left[\beta^2(K_2-K_1)+K_1\right]+2mgP_{max}[\beta(K_2-K_1)+K_1]}{K_1K_2A_{tfla}\alpha f_t} \\ w_0 = w_c/\lambda \end{cases} \tag{19}$$

4. Fracture Criterion of Double K

4.1. Calculation of Double K Coefficients

As is well-known, the relationship among $K_{IC}{}^{ini}$, $K_{IC}{}^{un}$, and $K_{IC}{}^{c}(\Delta a_c)$ is shown in Equation (20). The critical cohesive fracture toughness is represented by $K_{IC}{}^{c}(\Delta a_c)$, and the critical extension length of cracks under the maximum loading P_{max} is denoted by Δa_c, where $\Delta a_c = a_c - a_e$. Here, the equivalent stress-free cracking is denoted by a_e, and the critical equivalent cracking length is denoted by a_c, as shown in Table 3.

$$K_{IC}^{un} = K_{IC}^{ini} + K_{IC}^{c}(\Delta a_c) \tag{20}$$

According to the reference [26], the I-type fracture toughness of the specimen subjected to the four-point bending test can be calculated by Equation (21).

$$K_{IC} = \sigma_F \sqrt{\pi a} F(a/h) \tag{21}$$

In Equation (21), the maximum positive stress in the cross-section of the specimen is denoted by σ_F, which is calculated according to Equation (22); The extension length of the cracking is denoted by a; $F(a/h)$ is denoted as a dimensionless parameter related to I-Type fracture, which is calculated according to Equation (23).

$$\sigma_F = 6M/bh^2 = 3(P_E + mg)(d_1 - d_2)/\left(2bh^2\right) \tag{22}$$

$$F(a/h) = 1.122 - 1.40(a/h) + 7.33(a/h)^2 - 13.08(a/h)^3 + 14.0(a/h)^4 \tag{23}$$

The initiated fracture toughness $K_{IC}{}^{ini}$ and unstable fracture toughness $K_{IC}{}^{un}$ are computed by substituting the initiated loading P_{ini} and P_{max} into Equation (22) to calculate the normal stress σ_F, and then substituting the corresponding equivalent cracking length a into Equation (21). However, it was generally found that the P_{ini} and critical equivalent cracking length a_c were difficult to measure during testing. Consequently, it was proposed to first calculate $K_{IC}{}^{un}$ and $K_{IC}{}^{c}(\Delta a_c)$, and $K_{IC}{}^{ini}$ can then be calculated by subtracting $K_{IC}{}^{c}(\Delta a_c)$ from $K_{IC}{}^{un}$.

The $K_{IC}{}^{un}$ can be calculated based on a_c and P_{max} as defined in Figure 9c. Since the specimen exhibits a small nonlinear region in the load–displacement curve in Figure 5, it is assumed that this nonlinear behavior is caused by the extension of the cohesive cracking. Consequently, the critical equivalent cracking length a_c can be calculated using the principle of linear superposition. First, three data points of the load P_E and the corresponding *CMOD* within the elastic section of the P_E-*CMOD* curves for each specimen are selected. The three normal stresses σ_Fs are calculated using the selected three P_Es according to Equation (22). Subsequently, the three elastic moduli E^es are calculated by substituting σ_F and the corresponding *CMOD* values into Equation (24). The average value of the three E^es is taken as the effective elastic modulus of the specimen. Finally, a_c can be calculated by substituting the effective elastic modulus E^e, P_{max}, and the corresponding *CMODc* into Equation (21).

$$CMOD = 4\sigma a V(a/h)/E^e \tag{24}$$

$$V(a/h) = 0.8 - 1.7(a/h) + 2.4(a/h)^2 + 0.66(1 - a/h)^2 \tag{25}$$

The cohesive fracture toughness $K_{IC}{}^{c}(\Delta a)$ can be calculated by numerically integrating the cohesive stress $\sigma(x)$ and the stress intensity factor K_I over the path of the cohesive crack extension, as shown in Equation (26). The equation of the K_I is given in Equation (27), and the geometric simplified function $N(x/a, a/h)$ is given by Equation (28).

$$K_I^c = \int_{a_e}^{a} \sigma(x) K_I dx \tag{26}$$

$$K_I = -\frac{2}{\sqrt{\pi a}} N\left(\frac{x}{a}, \frac{a}{h}\right) \tag{27}$$

$$N\left(\tfrac{x}{a}, \tfrac{a}{h}\right) = \frac{3.52(1-x/a)}{(1-a/h)^{1.5}} - \frac{4.35-5.28x/a}{(1-a/h)^{0.5}} + \left(\frac{1.30-0.30(x/a)^{1.5}}{\left[1-(x/a)^2\right]^{0.5}} + 0.83 - 1.76(x/a)\right) \times \left[1-(1-x/a)\tfrac{a}{h}\right] \tag{28}$$

The cohesive stress distribution at the crack tip is depicted in Figure 11. After the equivalent cracking is initiated, the cohesive cracking is divided into two extension stages: the stable extension stage ($a_e \le a \le a_c$) and the instability extension stage ($a_c \le a \le a_{wo}$). As shown in Figure 11a, the cohesive stress is linearly distributed along the cohesive cracking, and the cohesive stress distribution function $\sigma(x)$ can be calculated according to Equation (29). The equation of $\sigma(w)$ is shown in Equation (1). As shown in Figure 11b, the distribution of the cohesive stress is bilinear, and the cohesive stress distribution function, $\sigma(x)$, can be calculated according to Equation (30).

$$\sigma(x) = \sigma(w) + [f_t\prime - \sigma(w)](x - a_e)/(a - a_e) \quad a_e \le x \le a \tag{29}$$

$$\sigma(x) = \begin{cases} \sigma_1(x) = \sigma(w) + [\sigma_c - \sigma(w)](x - a_e)/[a - (a_e + \Delta a_c)] & a_e \le x \le a - \Delta a_e \\ \sigma_2(x) = \sigma_c + (f_t' - \sigma_c)(x - a + \Delta a_c)/\Delta a_c & a - \Delta a_c \le x \le a \end{cases} \tag{30}$$

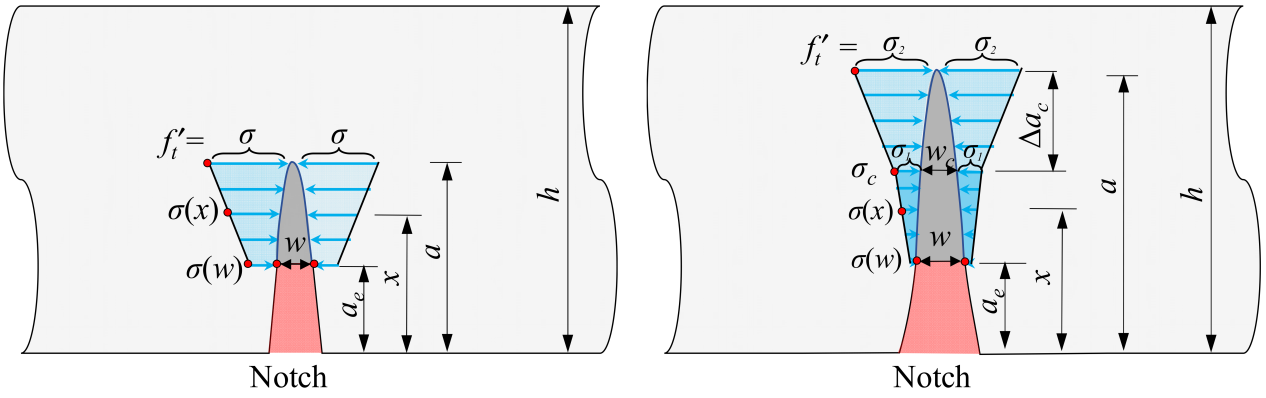


Figure 11. Cohesive stress distribution: (**a**) Before critical cracking length; (**b**) after critical cracking length.

For a known test load-deflection curve of a specimen, the calculation flowchart for determining the coefficients of the proposed bilinear softening model is shown in Figure 12 and is described as follows:

Step 1: The effective elastic modulus E^e is calculated by selecting the data points of P_Es and corresponding *CMOD* from the P_E-*CMOD* curve and substituting into Equations (22) and (24);

Step 2: The critical equivalent crack length a_c is calculated by substituting the E^e, P_{max}, and the corresponding $CMOD_c$ into Equation (21);

Step 3: The unstable fracture toughness ${K_{IC}}^{un}$ is calculated by substituting P_{max} and a_c into Equations (21)–(23);

Step 4: The cohesive stress distribution $\sigma(x)$ is calculated by using Equation (29) for the stable extension stage and Equation (30) for the unstable extension stage;

Step 5: The cohesive fracture toughness $K_{IC}{}^{c}(\Delta a)$ is calculated by using the cohesive stress $\sigma(x)$ computed in accordance with Equations (26)–(28) and stress intensity factor K_I through numerical integration along the crack extension path;

Step 6: The critical cohesive fracture toughness $K_{IC}{}^{c}(\Delta a_c)$ is calculated using the Δa_c obtained in Step 5;

Step 7: The initial fracture toughness $K_{IC}{}^{ini}$ is calculated by subtracting the $K_{IC}{}^{c}(\Delta a_c)$ from the $K_{IC}{}^{un}$ as determined in Step 3.

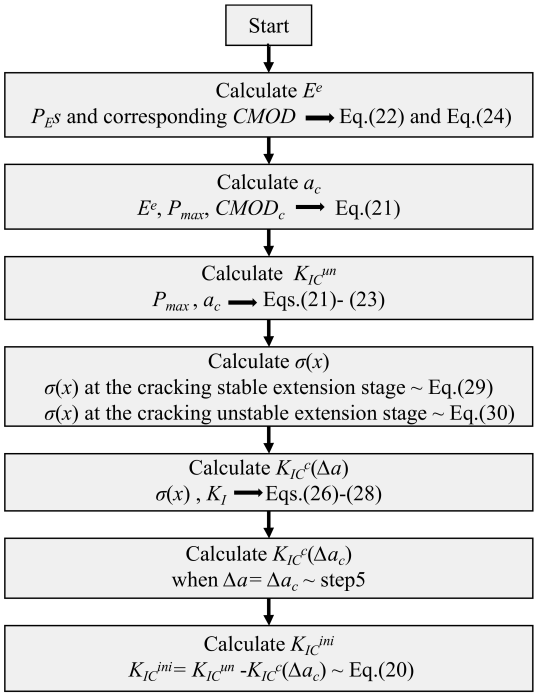


Figure 12. Calculation flow of $K_{IC}{}^{ini}$.

This calculation method can be applied to any specimen with a known load-deflection curve. The calculated parameters for the CEMI specimens are shown in Table 6. As indicated, the maximum errors between the experimental and predicted results are 4.92% for $\Delta a_c{}'$ and 8.19% for $K_{IC}{}^{ini\prime}$, respectively. This implies that the double-*K* values of CEMI specimens can be predicted by the proposed calculation method with good accuracy.

Table 6. Comparisons between predicted and test results.

Specimen	Test Data			Calculated Data					
	$\Delta a_c{}'$ mm	$K_{IC}{}^{ini\prime}$ MPa.mm$^{0.5}$	E^e GPa	Δa_c mm	$K_{IC}{}^{c}$	$K_{IC}{}^{un}$ MPa.mm$^{0.5}$	$K_{IC}{}^{ini}$	$\Delta a_c{}'/\Delta a_c$	$K_{IC}{}^{ini\prime}/K_{IC}{}^{ini}$
PB0%-1	18.76	0.68	27.81	18.01	−0.49	1.23	0.73	1.04	0.93
PB0%-2	16.36	0.72	25.27	17.05	−0.43	1.20	0.78	0.96	0.92
PB0%-3	15.56	0.69	24.15	15.33	−0.43	1.15	0.72	1.02	0.96
PB20%-1	13.21	0.75	36.92	13.86	−0.36	1.14	0.78	0.95	0.96
PB20%-2	12.69	0.76	38.75	13.23	−0.36	1.16	0.80	0.96	0.95
PB20%-3	12.72	0.76	38.98	13.18	−0.38	1.18	0.80	0.97	0.95
PB40%-1	13.90	0.77	27.74	14.57	−0.38	1.21	0.83	0.95	0.93
PB40%-2	14.88	0.80	29.75	15.58	−0.40	1.26	0.86	0.96	0.93
PB40%-3	12.88	0.78	27.39	13.26	−0.35	1.16	0.81	0.97	0.96

The proposed Double-K fracture calculation method is established based on the linear superposition principle and the bilinear cohesive zone model and is specifically formulated for Mode I fracture of the concrete–epoxy mortar interface. The method assumes that the

total stress intensity factor can be decomposed into the initial fracture toughness and the cohesive fracture toughness, and that the cohesive stress–crack opening relationship can be described by a bilinear softening law. In addition, the concrete and epoxy mortar are treated as macroscopically homogeneous materials.

It should be noted that the proposed method has certain limitations. First, the model is calibrated using quasi-static four-point bending tests and is mainly applied to Mode I-dominated fracture. Therefore, the calibrated parameters cannot be directly extended to Mode II or mixed-mode fracture without further validation. Second, when applied to other specimen geometries, interface materials, surface treatments, or loading conditions, the relevant parameters, especially the toughening factor α, should be recalibrated based on corresponding experimental data. For dynamic, fatigue, or long-term environmental loading conditions, additional tests are required to verify and extend the applicability of the proposed method.

4.2. Resistant Curve K_R

As expressed in Equation (31), the resistance to cracking, $K_R(\Delta a)$, is defined as the sum of ${K_{IC}}^{ini}$ and ${K_{IC}}^{c}(\Delta a)$. The calculated K_R curves of CEMI specimens are depicted in Figure 13a. As shown, the K_R curves of the specimens were significantly improved after the interface was pre-coated with epoxy solution. Specifically, the cohesive stresses σs of the PB20% and PB40% specimens were much larger than those of the normal specimen until Δa reached approximately 12.87 mm. However, the differences between these two pre-coated specimens (PB20% and PB40%) and the normal specimen were reduced beyond this point. Additionally, no significant differences in cohesive stress σ and resistance curve K_R were observed between the PB20% and PB40% specimens from the peak loading stage, as shown in Figure 13a.

The values of ${K_{IC}}^{ini}$, ${K_{IC}}^{un}$, and ${K_{IC}}^{o}$ for specimens at the cracking initiation stage, unstable extension stage (maximum load, P_{max}), and failure stage are depicted in Figure 13b. As shown, compared with the PB0% specimen without pre-coating, the ${K_{IC}}^{ini}$ values of the pre-coated specimens (PB20% and PB40%) were improved by 6.7% and 12.1%, respectively; whereas the ${K_{IC}}^{un}$ values were improved by -3.0% and 1.5%, respectively; and the ${K_{IC}}^{o}$ values were improved by 20.0% and 17.4%, respectively. This improvement was attributed to the pre-coating using the epoxy solution, which enhanced the bridge link effect, thereby accumulating more cohesive energy at the cracking tip. As a result, both the cracking initiation toughness and the cohesive toughness at the cracking initiation and stable extension stages were significantly improved.

The critical crack extension length at cracking unstable extension Δa_cs and at failure Δa_{w0}s are shown in Figure 13c. As illustrated, the Δa_c values of PB20% and PB40% specimens were decreased by 20.1% and 13.9%, respectively, compared with that of the PB0% specimen; while the Δa_{w0} values were increased by 32.0% and 26.5%, respectively. This was attributed to the enhanced bridge links at the interface from the pre-coating, by which more cohesive energy was accumulated at the crack tip, crack initiation was made more difficult, and the stable extension length of the crack was shortened. During the unstable extension stage, greater resistance was encountered by crack propagation due to the presence of the bridge links. Consequently, more energy was required for the failure of the specimen, resulting in a significant increase in the crack extension length. In contrast, quick failure was exhibited by the specimens without pre-coating due to the lack of bridge links at the interface, resulting in lower cohesive energy accumulation at the crack tip.

$$K_R(\Delta a) = K_{IC}^{ini} + K_{IC}^{c}(\Delta a) \tag{31}$$

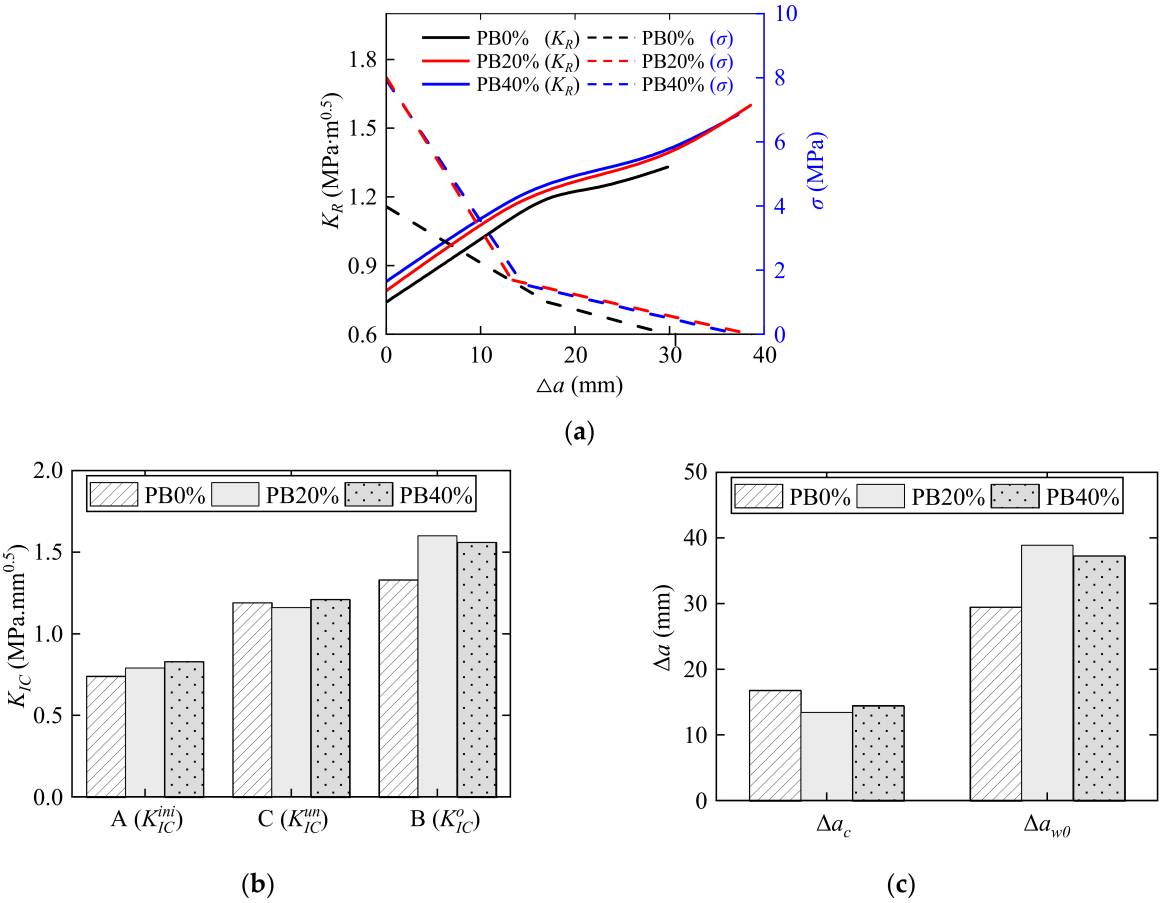


Figure 13. Comparison of K_R: (**a**) K_R-Δa curves; (**b**) fracture toughness K_{IC}; (**c**) equivalent crack extension length Δa.

5. Conclusions

The fracture performance of CEMI specimens pre-coated with epoxy solutions at different concentrations was investigated through four-point bending tests on nine specimens. A simplified parameter determination method for the bilinear softening model was proposed based on the tri-linear stiffness model. By combining this bilinear softening model with linear elastic fracture mechanics, the crack initiation toughness, unstable toughness and the K_R resistance curve for the interfacial crack were determined. Meanwhile, the influence of the pre-coating concentration on the interface toughening mechanism and the crack evolution within the fracture process zone (FPZ) was revealed using DIC technology and SEM micro-analysis. The following conclusions were drawn from the results of this investigation:

1. The crack initiation location and the crack propagation path were effectively measured by the DIC. The error of the crack initiation load P_{ini} between the traditional method using gages and the DIC results was found to be less than 5.0%;
2. Scanning electron microscope analysis revealed that the bridging effect was improved by the pre-coating of specimens through the filling of the microscopic defects on the concrete surface, by which the cracking resistance of the CEMI specimens was improved;
3. A general method for determining the parameters of the bilinear softening model was proposed. The error in the critical crack tip opening displacement w_c between the DIC and predicted results was found to be no more than 8.09%. Additionally, the error of the crack initiation toughness $K_{IC}{}^{ini}$ between the calculated results and test results was smaller than 8.19%;

4. Compared to the PB0% specimen without pre-coating, the cracking initiation toughness $K_{IC}{}^{ini}$s values for the pre-coated PB20% and PB40% specimens were increased by 6.7% and 12.1%, respectively. The fracture toughness at failure $K_{IC}{}^{o}$ was increased by 20.0% and 17.4%, and the critical crack extension length Δa_{w0}s was increased by 32.0% and 26.5%, respectively;
5. The improvement in fracture performance of the CEMI is primarily attributed to the pre-coating, by which the bridging effect at the interface is enhanced, and the interfacial cracking resistance is significantly improved.

This study has the following limitations: the experimental parameter range was limited, as only three epoxy resin concentrations and a fixed concrete strength grade were considered; the micro-scale toughening mechanism was only described qualitatively; and the study was based solely on quasi-static loading. To address these limitations, future research will be focused on three key areas: (1) multi-parameter tests will be conducted to verify the general applicability of the proposed method; (2) micro-characterization techniques will be employed to establish a quantitative relationship between the defect distribution and the fracture parameters; (3) environmental and fatigue performance studies will be performed to evaluate the long-term stability.

Author Contributions: Z.H.: conceptualization, methodology, visualization, investigation; Z.M.: software, data curation, writing—original draft preparation; Y.Y.: conceptualization, methodology, writing—original draft preparation, investigation, and writing—reviewing and editing. All authors have read and agreed to the published version of the manuscript.

Funding: This research was funded by the Department of Transportation of Zhejiang Province, grant number 2023018 and the APC was funded by the Department of Transportation of Zhejiang Province, grant number 2023018.

Institutional Review Board Statement: Authors state that the research was conducted according to ethical standards.

Data Availability Statement: All data and models generated or used during this study are available from the corresponding author by request.

Conflicts of Interest: The authors declare that there is no conflict of interest regarding the publication of this paper.

Nomenclature

A_{tfla}	cross-sectional area of the specimen, mm^2
a	equivalent crack length, mm
a_c	equivalent crack length at maximum load, mm
a_e	equivalent stress-free crack length, mm
a_f	equivalent free crack length, mm
a_{w0}	equivalent crack length when $w = w_0$, mm
a_0	pre-cut notch height, mm
a_0/h	initial crack-height ratio
b	width of the specimen, mm
$CMOD$	crack mouth opening displacement, mm
$CMOD_c$	crack mouth opening displacement under maximum load, mm
$CTOD$	crack tip opening displacement, mm
$CTOD_c$	crack tip opening displacement under maximum load, mm
D	mid-span deflection, mm
D_0	vertical deflection under the loading point when external load $P_E = 0$, mm
D_c	vertical deflection under the loading point at the maximum load, mm
D_{max}	vertical deflection under the loading point at the final failure, mm

D_M	vertical deflection under the loading point, mm
d_1	span of lower constraint support, mm
d_1/h	Span-to-depth ratio
d_2	span of upper loading support, mm
DIC	digital image correlation technology
E^e	elastic modulus, MPa
$V(a/h)$	a dimensionless parameter related to *CMOD*
$N(x/a,a/h)$	a dimensionless parameter related to K_I
$F(a/h)$	a dimensionless parameter related to I-Type fracture
$f(D_M)$	P_E-D_M curves
$f(D_M)'$	P-D_M curves
f_t	tensile strength of concrete, MPa
f_t'	equivalent tensile strength of concrete, MPa
G_f	total fracture energy based on the triple-folding model, J/m^2
G_{fb}	crack bridging fracture energy based on the triple-folding model, J/m^2
G_{fu}	micro-crack fracture energy based on the triple-folding model, J/m^2
G_f'	total fracture energy obtained by integrating the load–displacement curves, J/m^2
G_{fb}'	crack bridging fracture energy obtained by integrating the load–displacement curves, J/m^2
G_{fu}'	micro-crack fracture energy obtained by integrating the load–displacement curves, J/m^2
h	depth of the specimen, mm
K	the stress intensity factor, MPa.mm$^{0.5}$
K_R	the crack extension resistance, MPa.mm$^{0.5}$
K_{IC}^{ini}	initiation toughness for I-Type cracks, MPa.mm$^{0.5}$
K_{IC}^{un}	unstable fracture toughness for I-Type cracks, MPa.mm$^{0.5}$
$K_{IC}^{c}(\Delta a)$	cohesive toughness, MPa.mm$^{0.5}$
$K_{IC}^{c}(\Delta a_c)$	critical cohesive toughness, MPa.mm$^{0.5}$
K_{IC}^{0}	cohesive toughness when $w = w_0$, MPa.mm$^{0.5}$
$K_{IC}^{ini\prime}$	initiation toughness for I-Type cracks obtained from the experiment, MPa.mm$^{0.5}$
l	length of the specimen, mm
M	the bending moment in the pure bending section, N·m
P	total applied load, kN
P_E	applied load under external forces, kN
P_G	equivalent additional load representing the self-weight of the specimen and distribution beam, kN
P_{ini}'	crack initiation load obtained from the strain gauge method, kN
P_{ini}	crack initiation load obtained from the DIC method, kN
P_{max}	maximum load, kN
t_e	epoxy mortar layer thickness, mm
w	crack tip opening displacement, mm
w_c	critical crack tip opening displacement, mm
w_0	crack tip opening displacement of fully developed virtual equivalent crack, mm
W_T	total work done by external forces, J
W_{fu}	external work driving the development of micro-cracks, J
W_{fb}	external work driving crack bridging fracture, J
W_L	work done as the deflection changes from D_0 to D_{max} by P_G, J
x	distance from the bottom of the specimen to any point on the equivalent crack, mm
α	toughening factor
β	the ratio of micro-crack fracture energy to total fracture energy
λ_1,λ_2,λ_3	bilinear softening parameter calculation coefficients
σ	equivalent cohesive stress of the crack, MPa
σ_c	critical equivalent cohesive stress of the crack, MPa
$\sigma(x)$	equivalent tress distribution function, MPa

$\sigma(w)$	equivalent cohesive stress at the crack tip, MPa
σ_F	maximum tensile stress at the cross-section of a four-point bending specimen, MPa
Δa	equivalent crack extension length, mm
Δa_c	critical equivalent crack extension length, mm
$\Delta a_c{}'$	critical equivalent crack extension length obtained from the experiment, mm
Δa_{w0}	equivalent crack propagation length when $w = w_0$, mm
$\Delta a_A{}'$	cohesive crack length at the initiation point, mm
$\Delta a_M{}'$	cohesive crack length at the point M, mm
$\Delta a_B{}'$	cohesive crack length at the fracture failure point, mm

References

1. Ishaq, S.; Jang, Y.; An, D.; Jeong, Y.; Youn, I. A Novel Approach to Quantifying the Failure Modes of Concrete-Epoxy Interface. *Materials* **2023**, *16*, 2376. [CrossRef] [PubMed]
2. Kumar, P.; Kasar, A.A.; Chaudhary, S. Numerical Analysis of Interfacial Failure Mechanism in Bonded Steel-Concrete Composite Connections. *Int. J. Steel Struct.* **2023**, *23*, 1279–1293. [CrossRef]
3. Chen, P.Q.; Li, Y.Q.; Zhou, X.J.; Wang, H.; Li, J. Study on the Bond Performance of Epoxy Resin Concrete with Steel Reinforcement. *Buildings* **2024**, *14*, 2905. [CrossRef]
4. Hang, Z.Y.; Mi, Z.K.; Wu, Y.F.; Wang, J.H.; Yu, Y. Fracture performance of concrete-epoxy mortar interface subjected to bending and shear: Experimental and numerical study. *J. Bridge Eng.* **2024**, *97*, 110887. [CrossRef]
5. Hang, Y.; He, K.S.; Zhao, W.; Yu, Y. Fracture properties of a concrete-epoxy mortar interface with precoating treatment applied through image correlation technology. *Constr. Build. Mater.* **2023**, *370*, 130640. [CrossRef]
6. Daneshvar, D.; Behnood, A.; Robisson, A. Interfacial bond in concrete-to-concrete composites: A review. *Constr. Build. Mater.* **2022**, *359*, 129195. [CrossRef]
7. Li, Y.; Zhuang, X.L.; Li, Z.H.; Wang, R.J.; Xiong, X.B. The mechanical properties of the interface between concrete-epoxy mortar: Splitting tensile vs. direct shear testing. *Constr. Build. Mater.* **2024**, *422*, 135809. [CrossRef]
8. Zhou, A.; Buyukozturk, O.; Lau, D. Debonding of concrete-epoxy interface under the coupled effect of moisture and sustained load. *Cem. Concr. Compos.* **2017**, *80*, 287–297. [CrossRef]
9. Jeong, Y.; Lopez, M.M.; Bakis, C.E. Effects of Sustained Loading and Temperature on a Concrete-Epoxy Bonded Interface. *J. Mater. Civil Eng.* **2020**, *32*, 04020016. [CrossRef]
10. Lee, J.; Artun, K.; Bakis, C.E.; Lopez, M.M.; Boothby, T.E. Changes in fracture energy at FRP-concrete interfaces following indoor and outdoor exposure with sustained loading. *Constr. Build. Mater.* **2023**, *392*, 131905. [CrossRef]
11. Liang, H.J.; Li, S.; Lu, Y.Y.; Yang, T. The combined effects of wet-dry cycles and sustained load on the bond behavior of FRP-concrete interface. *Polym. Compos.* **2019**, *40*, 1006–1017. [CrossRef]
12. Yu, Y.; He, K.S.; Hang, Z.Y.; Liu, W.; Zhao, W. Effects of adhesive layer thickness on the fracture properties of a concrete-epoxy resin interface. *Theor. Appl. Fract. Mech.* **2024**, *130*, 104239. [CrossRef]
13. Ren, Y.; Gao, Z.Q.; Xia, M.Y.; Guo, R. Study on bonding behavior of FRP grid-ECC composite layer and concrete with quantitative interface treatment. *Eng. Struct.* **2023**, *294*, 116768. [CrossRef]
14. Zhao, W.; Jiang, Y.X.; Yu, Y.; Liu, W. Use of digital image correlation to confirm the enhancement of concrete–epoxy resin mortar adhesion through surface precoating treatment. *Constr. Build. Mater.* **2021**, *295*, 123512. [CrossRef]
15. Bahraq, A.A.; Al-Osta, M.A.; Obot, I.B.; Al-Amoudi, O.S.B.; Saleh, T.A.; Maslehuddin, M. Improving the adhesion properties of cement/epoxy interface using graphene-based nanomaterials: Insights from molecular dynamics simulation. *Cem. Concr. Compos.* **2022**, *134*, 104801. [CrossRef]
16. Luo, Q.; Li, Y.Y.; Zhang, Z.; Peng, X.J.; Geng, G.Q. Influence of substrate moisture on the interfacial bonding between calcium silicate hydrate and epoxy, Construct. *Build. Mater.* **2022**, *320*, 126252. [CrossRef]
17. Zhang, Z.H.; Zhao, T.L.; Wang, X. Mesoscale modelling of concrete damage in FRP-concrete debonding failure. *Eng. Struct.* **2023**, *289*, 116310. [CrossRef]
18. Wang, X.; Zhao, T.L.; Guo, J.L.; Zhang, Z.H.; Song, X.G. Mesoscale modelling of the FRP-concrete debonding mechanism in the pull-off test. *Compos. Struct.* **2023**, *309*, 116726. [CrossRef]
19. Lou, B.X.; Ma, F.H. Crack extension resistance of steam-cured concrete under different curing temperature conditions. *Theor. Appl. Fract. Mech.* **2022**, *119*, 103331. [CrossRef]
20. Wang, B.; Zhu, E.Y.; Zhu, C.Q.; Zhang, Z. Effect of microstructural characteristics of lightweight aggregate concrete on fracture parameters of three-point bending notched beams. *Theor. Appl. Fract. Mech.* **2022**, *121*, 103545. [CrossRef]
21. Yin, Y.Y.; Hu, S.W.; Liang, C.F.; Sun, Y.Y. Crack extension resistance for a general three-point bending concrete beam. *Eng. Fract. Mech.* **2023**, *290*, 109490. [CrossRef]

22. Yin, Y.Y.; Jing, Z.W.; Hu, S.W.; Liang, C.F.; Hou, G.; Sun, Y.Y.; Wang, Y. Study on crack propagation behaviors of three-point bending concrete beams with small span-depth ratios. *Theor. Appl. Fract. Mech.* **2024**, *133*, 104638. [CrossRef]
23. Yin, Y.Y.; Qiao, Y.M.; Hu, S.W. Determining concrete fracture parameters using three-point bending beams with various specimen spans. *Theor. Appl. Fract. Mech.* **2020**, *107*, 102465. [CrossRef]
24. Guan, J.F.; Wang, Y.G.; Xie, C.P.; Li, L.L.; Cao, Z. Non-linear fracture analysis of hematite concrete considering micropore diameter and porosity. *Eng. Fract. Mech.* **2024**, *309*, 110328. [CrossRef]
25. Yuan, W.Y.; Dong, W.; Zhang, B.S.; Yu, D.H. Determination of SIFs and application of a SIF-based fracture criterion for concrete-rock interface under sustained loading. *Cem. Concr. Compos.* **2024**, *145*, 105342. [CrossRef]
26. Liu, W.; Feng, P.; Huang, J. Bilinear softening model and double K fracture criterion for quasi-brittle fracture of pultruded FRP composites. *Compos. Struct.* **2017**, *160*, 1119–1125. [CrossRef]
27. Yuan, W.Y.; Dong, W.; Zhang, B.S.; Zhong, H. Investigations on fracture properties and analytical solutions of fracture pa-rameters at rock-concrete interface. *Constr. Build. Mater.* **2021**, *300*, 124040. [CrossRef]
28. Biswal, S.; Singh, G. Determination of fracture toughness and traction-separation relation in Mode I/II of a natural quasi-brittle orthotropic composite using multi-specimen approach. *Eng. Fract. Mech.* **2023**, *282*, 109163. [CrossRef]
29. Cintra, G.G.; Vieira, J.D.; Cardoso, D.C.T.; Keller, T. Mode I and Mode II fracture behavior in pultruded glass fiber-polymer—Experimental and numerical investigation. *Compos. Part. B-Eng.* **2023**, *266*, 110988. [CrossRef]
30. Yan, X.Q.; Guo, X.M.; Gao, Y.F.; Lin, Y.; Zhang, N.N.; Zhao, Q.L. Mode-II fracture toughness and crack propagation of pultruded carbon Fiber-Epoxy composites. *Eng. Fract. Mech.* **2023**, *279*, 109042. [CrossRef]
31. Yu, Y.; Xin, R.X.; Zeng, W.H.; Liu, W. Fracture resistance curves of wood in the longitudinal direction using digital image correlation technique. *Theor. Appl. Fract. Mech.* **2021**, *114*, 102997. [CrossRef]
32. Xu, Y.; Zhao, G.L.; Li, X.; Wu, B.B.; Xia, K.W. Influences of notch width and notch-tip angle on the fracture toughness measurement using the semi-circular bend (SCB) specimen. *Eng. Fract. Mech.* **2023**, *281*, 109098. [CrossRef]
33. Wu, Y.; Yin, T.B.; Zhuang, D.D.; Chen, Y.J.; Ma, J.X.; Guo, W.X. Initial and unstable fracture toughness of quartz-diorite rock under mixed mode I/II loading: Experimental and numerical investigation. *Theor. Appl. Fract. Mech.* **2023**, *127*, 104079. [CrossRef]
34. Tada, H.; Paris, P.C.; Irwin, G.R. *The Stress Analysis of Cracks Handbook*; ASME Press: New York, NY, USA, 2000.
35. *GB50010-2010*; Concrete Structure Design Code. China Ministry of Construction: Beijing, China, 2010.
36. *GB/T50081-2002*; Testing Methods of Mechanical Properties of Ordinary Concrete. China Ministry of Construction: Beijing, China, 2002.
37. *DL/T 5193-2004*; Technical Code of Epoxy Resin Mortar. National Development and Reform Commission: Beijing, China, 2004.
38. Yu, Y.; Zeng, W.H.; Liu, W.; Zhang, H.; Wang, X.H. Crack propagation and fracture process zone (FPZ) of wood in the longitudinal direction determined using digital image correlation (DIC) technique. *Remote Sens.* **2019**, *11*, 1562. [CrossRef]
39. Zhao, W.; Yu, Y.; Xie, Q.S. Nonuniform interface failure of steel-concrete composite structures bonded using epoxy resin mortar. *Eng. Struct.* **2019**, *184*, 447–458. [CrossRef]
40. Hillerborg, A.; Modeer, M.; Petersson, P. Analysis of crack formation and crack growth in concrete by means of fracture mechanics and finite elements. *Cem. Concr. Res.* **1976**, *6*, 773–782. [CrossRef]
41. Guinea, G. Modelling the fracture of concrete: The cohesive crack. *Mater. Struct.* **1995**, *28*, 187–194. [CrossRef]
42. Mehrab, A.H.; Esfahani, M.R. Experimental study on size effect and fracture properties of polypropylene fiber reinforced lightweight aggregate concrete. *Period. Polytech. Civ. Eng.* **2022**, *66*, 1278–1293. [CrossRef]
43. Swartz, S.E.; Yap, S.T. The influence of dead load on fracture energy measurements using the RILEM method. *Mater. Struct.* **1988**, *21*, 410–415. [CrossRef]

Disclaimer/Publisher's Note: The statements, opinions and data contained in all publications are solely those of the individual author(s) and contributor(s) and not of MDPI and/or the editor(s). MDPI and/or the editor(s) disclaim responsibility for any injury to people or property resulting from any ideas, methods, instructions or products referred to in the content.